JACS
JOURNAL OF THE AMERICAN CHEMICAL SOCIETY
pubs.acs.org/JACS
Article

Imaging Purely Nuclear Quantum Dynamics in Molecules by Combined X-ray and Electron Diffraction

Haiwang Yong,* Daniel Keefer, and Shaul Mukamel*

Cite This: *J. Am. Chem. Soc.* 2022, 144, 7796−7804
Read Online
ACCESS | Metrics & More | Article Recommendations | Supporting Information

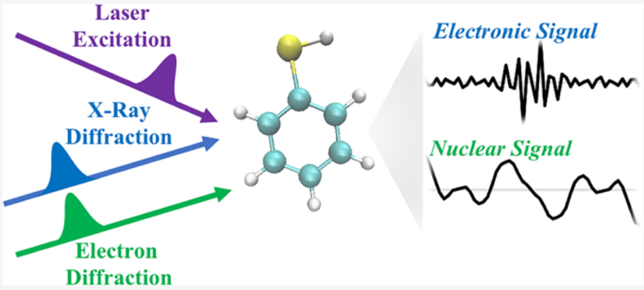

ABSTRACT: Monitoring the motions of atoms and molecules in the course of chemical processes is a central goal of femtochemistry. Optical spectroscopic signals are usually sensitive to electronic properties such as dipoles, polarizabilities, and electronic charge densities rather than to nuclear motions. In this theoretical study, we propose a novel measurement that solely and directly monitors the evolving nuclear wave packet and can thereby unambiguously image photochemical events in real time. We demonstrate how nuclear charge densities can be singled out by subtracting the ultrafast gas-phase X-ray and electron diffraction signals in the photodissociation of thiophenol as it passes through two conical intersections. This signal can reveal the shape and trajectory of the nuclear wave packets as well as the electronic coherences in the vicinity of conical intersections.

■ INTRODUCTION

Nuclear wave-packet dynamics in molecules is of fundamental interest for unraveling the mechanisms of elementary photophysical and photochemical events such as the passage through conical intersections (CIs).[1−4] Key photochemical molecular motions happen on the femtosecond (10^{-15} s) timescale. Ultrashort broad-bandwidth optical pulses can generate a coherent superposition of many vibrational states that initiates light-driven chemical reactions described by coherent nuclear wave-packet motions.[5−8] Yet, the direct measurement of purely nuclear wave packets in a polyatomic molecule remains challenging since probe pulses in spectroscopy and imaging usually interact with electrons rather than the nuclei themselves. Nuclear densities have long been detected by neutron scattering on a timescale of microseconds[9,10] with potential to approach the picosecond timescale[11] but still misses the much faster elementary chemical reaction events.

In the present simulation study, we demonstrate that purely nuclear wave-packet dynamics and its passage through CIs can be directly imaged by subtracting the ultrafast heterodyne-detected X-ray and electron diffraction signals. Time-resolved X-ray diffraction monitors the electronic charge density, whereas electron diffraction measures the total (electronic + nuclear) charge density. Both techniques have been broadly applied to measurement of the evolution of nuclear wave packets in excited states.[12−20] Previous experiments only determined the centroids of the wave-packet motions but could not capture the complete profile (*i.e.*, the shape and amplitude) of the evolving wave packets since it is often obscured by the diffuse electron density.[21] Homodyne-detected X-ray and electron diffraction have shown promising advantages, for example, in monitoring coherences that arise at CIs with X-ray diffraction[22] or obtaining mixed nuclear/electronic terms to reveal their coupling in electron diffraction.[23] A recent ultrafast electron diffraction experiment by Yang *et al.* disentangled the diffraction signals contributed from electronic and nuclear structural changes by investigating small-angle inelastic scattering and large-angle elastic scattering, respectively.[24] Since the nuclear structural changes measured in elastic electron scattering have two different origins (*i.e.*, the motion of molecular nuclei and the motion of atomic core electrons that are centered tightly around the nuclei), the wave-packet motion of purely molecular nuclei cannot be directly measured in conventional homodyne-detected diffraction. Here, we show that the purely nuclear charge density with a quantum treatment of nuclei can be obtained by subtracting these two heterodyne-detected diffraction measurements. Heterodyne-detected diffraction requires an additional reference wave that interferes with the photons/electrons scattered from the sample. The relative phase between two pulses must be controlled in order to recover the signal and its phase. Time-resolved heterodyne detection has been extensively studied for both X-ray[25−27] and electron diffraction[28,29] in the field of holographic imaging. It is

Received: February 2, 2022
Published: April 25, 2022

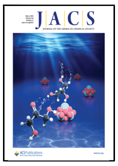

https://doi.org/10.1021/jacs.2c01311

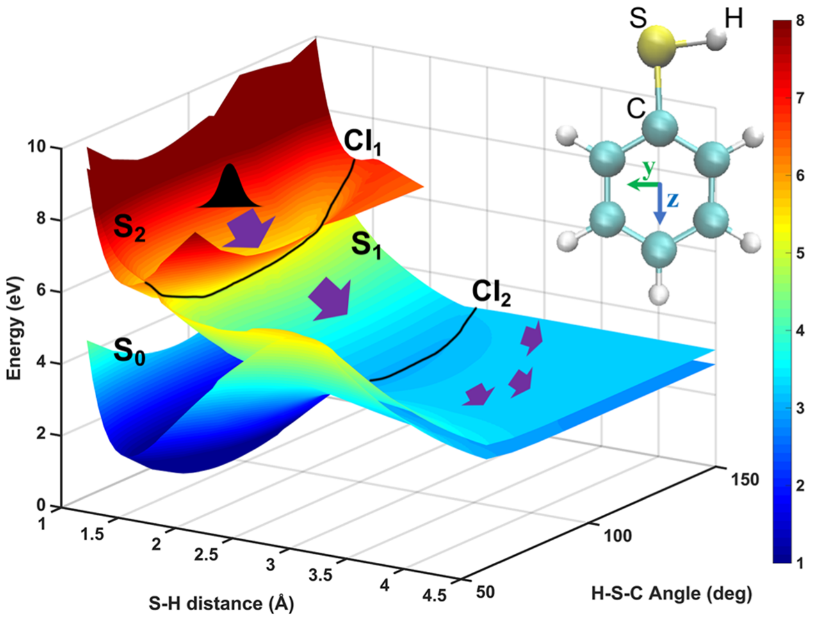

Figure 1. PESs of the S_2, S_1, and S_0 adiabatic electronic states of thiophenol in our two-dimensional nuclear space (S−H distance and H−S−C angle) calculated at the SA4-CAS(12,11)/6-311++G(d,p) level of theory. Two CIs (CI$_1$: S_2/S_1 and CI$_2$: S_1/S_0) are marked with black lines. Purple arrows sketch the photodissociation pathway of the nuclear wave packet initially prepared in S_2. Inset: molecular structure of thiophenol located in the $y-z$ plane.

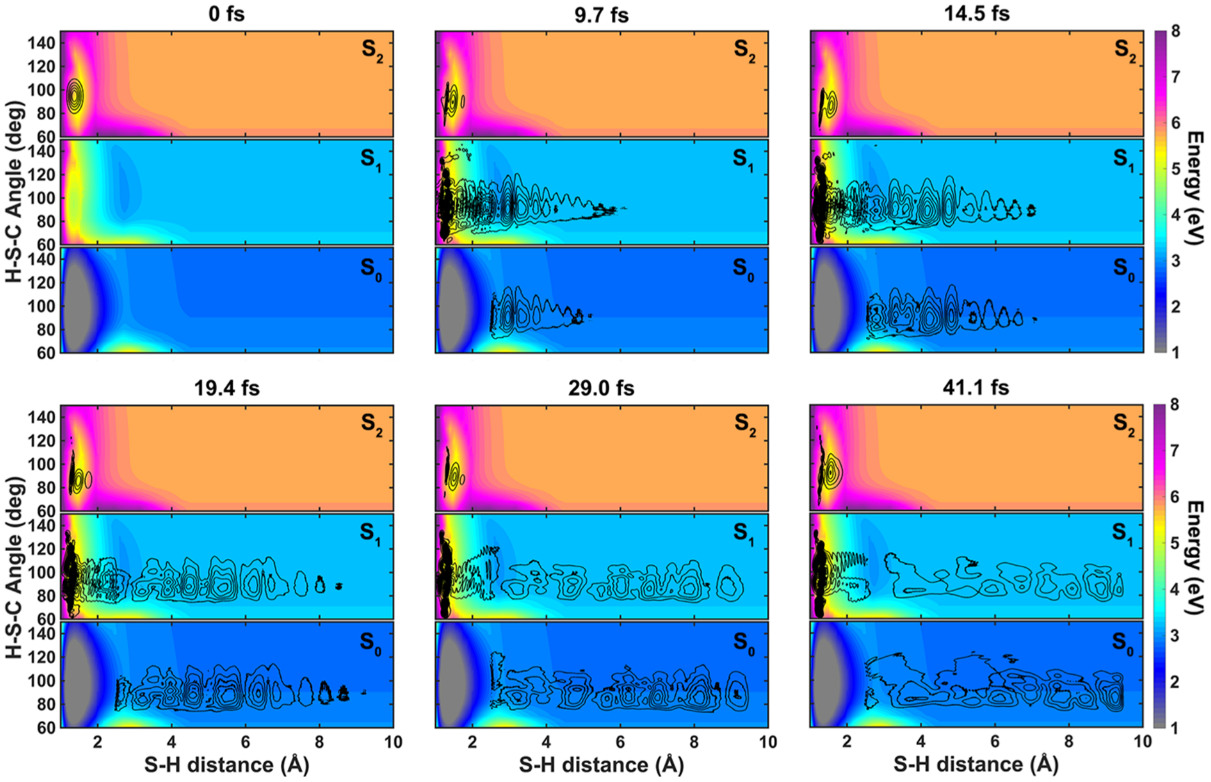

Figure 2. Simulated nuclear wave-packet dynamics at selected times t. Black contour lines are the nuclear wave-packet snapshots as a function of two-dimensional nuclear space (S−H distance and H−S−C angle) for S_2 (top), S_1 (middle), and S_0 (bottom) adiabatic electronic states. Color plots are two-dimensional PESs of the S_2, S_1, and S_0 adiabatic electronic states shown in Figure 1. The potential energy (eV) is represented by the color intensity (see color bar).

tempting to extend these techniques toward the imaging of ultrafast structural dynamics in molecules. Heterodyne-detected diffraction is challenging but can be greatly rewarding as it directly measures the time-evolving charge density of the molecule in momentum space. In contrast, homodyne diffraction occurs from expectation values of products of charge density operators. Heterodyne signals are thus linear in the charge densities, whereas homodyne signals are quadratic. The time-evolving nuclear charge density of the molecule in real space can be directly reconstructed by subtracting heterodyne-detected X-ray and electron diffraction patterns, which is not possible by standard (homodyne) measurements due to the mixed electron/nuclear terms in electron diffraction.[23] The two measurements can be performed separately as long as the chemical environment of the measured sample is maintained.

■ QUANTUM DYNAMICAL SIMULATIONS

We have applied this protocol to probe the photodissociation of thiophenol upon photoexcitation to the S_2 state (Figure 1). Previous studies have found two CIs along the S−H dissociation channels, S_2/S_1 CI near 1.5 Å and S_1/S_0 CI near 2.7 Å, in the course of this nonadiabatic relaxation process.[30−32] In addition to S−H stretching, the in-plane SH bending mode was found to be involved in the CI dynamics.[32] The adiabatic potential energy surfaces (PESs) of the three relevant electronic states in this two-dimensional nuclear space depicted in Figure 1 were calculated with *ab initio* electronic structure method (see details in the Supporting Information). At large S−H distances (>2 Å), the S_1 and S_0 PESs steeply rise at small H−S−C angles due to strong repulsion when the dissociating hydrogen atom is close to the carbon ring. Quantum dynamical simulations in the reduced-dimensional space of the two reactive coordinates were performed by numerically solving the time-dependent Schrödinger equation for nuclei on the adiabatic PESs including nonadiabatic couplings at the CIs, allowing for a fully quantum mechanical treatment of both electrons and nuclei in the nonadiabatic passage (details are given in the Supporting Information).

Figure 2 shows the simulated nuclear wave-packet dynamics at selected times *t*. Following the initial excitation at $t = 0$ which prepares the wave packet at the S_2 PES which is localized in both nuclear degrees of freedom, within 10 fs, it reaches the S_2/S_1 CI and relaxes to S_1, illustrated by the black contour lines appearing on the S_1 surface in Figure 2, 9.7 fs panel. During this process, a small portion of the wave packet (black contour lines on the S_0 surface in Figure 2, 9.7 fs panel) reaches the S_1/S_0 CI and starts to relax to S_0. Between 10 and 20 fs, the wave packet further evolves to longer S−H distances (Figure 2, 14.5 and 19.4 fs panels), eventually leading to ∼30 fs S−H bond breaking on both the S_1 and S_0 surfaces. The bond dissociation reaction in S_1 and S_0 continues to take place while the remaining portion of wave packet near the Franck−Condon region passes through the S_2/S_1 and the S_1/S_0 CIs. The nuclear wave packet rapidly spreads along both coordinates (S−H distance and H−S−C angle) within a few femtoseconds. This demonstrates the need to characterize the time-evolved spreading of the nuclear wave packet as described by nonadiabatic molecular dynamics approaches[33−35] for a complete understanding of the photodissociation dynamics.

■ THEORY OF HETERODYNE-DETECTED DIFFRACTION SIGNALS

The total time-dependent molecular wave function prepared by an optical excitation is expanded as

$$\Psi(\mathbf{r}, \mathbf{R}, t) = \sum_{g} c_g(t)\chi_g(\mathbf{R}, t)\varphi_g(\mathbf{r}, \mathbf{R}) \tag{1}$$

where g labels the adiabatic electronic states, $\chi_g(\mathbf{R}, t)$ is the normalized nuclear wave packet in the adiabatic electronic state $\varphi_g(\mathbf{r}, \mathbf{R})$, $\mathbf{r}$ and $\mathbf{R}$ are the electronic and nuclear coordinates, respectively, t is the time, and c_g is the electronic state amplitude. The heterodyne-detected single-molecule diffraction signal is[36]

$$S_{\mathrm{het}}(\mathbf{q}, T) \propto 2\mathcal{I}\int \mathrm{d}\, t A_{\mathbf{X}}(t - T)\mathbf{A}^{*}_{\mathbf{het}}(t - T)\tilde{S}_{\mathrm{het}}(\mathbf{q}, t) \tag{2}$$

where $\mathcal{I}$ is the imaginary part of the function, $\mathbf{q} = \mathbf{k}_{\mathbf{het}} - \mathbf{k}_{\mathbf{X}}$ is the scattering momentum, $\mathbf{A}_{\mathbf{X}}(t - T)$ is the X-ray/electron probe pulse vector potential at delay time T, $\mathbf{A}^{*}_{\mathbf{het}}(t - T)$ is the conjugate heterodyne reference X-ray/electron pulse, and $\tilde{S}_{\mathrm{het}}(\mathbf{q}, t)$ is the time-dependent molecular response

$$\begin{aligned}\tilde{S}_{\mathrm{het}}(\mathbf{q}, t) &= \langle\Psi(t)|\hat{\sigma}(\mathbf{q})|\Psi(t)\rangle\\ &= \sum_{gg'} \rho_{g'g}(t)\langle\chi_g(t)|\hat{\sigma}_{gg'}(\mathbf{q})|\chi_{g'}(t)\rangle\end{aligned} \tag{3}$$

Here, $\rho_{g'g}(t) = c_g^{*}(t)c_{g'}(t)$ and $\hat{\sigma}(\mathbf{q})$ is the Fourier transform of the total charge-density operator. The experimental requirements for the detection of the heterodyne signal have been discussed recently.[36] In brief, it requires two coincident, noncollinear pulses with a controlled relative phase. The scattering wave vector $\mathbf{q}$ can be scanned by varying the angle between the probe $\mathbf{A}_{\mathbf{X}}$ and the reference pulse $\mathbf{A}_{\mathbf{het}}$. Hereafter, we assume a very short (impulsive) probe and heterodyne reference pulses in eq 2 and focus on the time-dependent molecular response signal $\tilde{S}_{\mathrm{het}}(\mathbf{q}, t)$. The signal measured with a semi-impulsive pulse reflects the molecular response signal averaged within the finite pulse width (usually a few femtoseconds). This limits the temporal resolution, thereby losing important signals, especially of fast dynamical features at CIs. This problem can be overcome by the ongoing developments of both attosecond hard X-ray[37] and attosecond relativistic megaelectron volt electron pulses.[38]

Using the electronic charge-density operator $\hat{\sigma}^{\mathrm{E}}(\mathbf{q})$, the time-dependent X-ray heterodyne diffraction signal in eq 3 is written as

$$\begin{aligned}\tilde{S}^{\mathrm{XRD}}_{\mathrm{het}}(\mathbf{q}, t) &= \sum_{gg'} \rho_{g'g}(t)\langle\chi_g(t)|\hat{\sigma}^{\mathrm{E}}_{gg'}(\mathbf{q})|\chi_{g'}(t)\rangle\\ &= \sum_{g} \rho_{gg}(t)\langle\chi_g(t)|\hat{\sigma}^{\mathrm{E}}_{gg}(\mathbf{q})|\chi_g(t)\rangle\\ &\quad + \sum_{g\neq g'} \rho_{g'g}(t)\langle\chi_g(t)|\hat{\sigma}^{\mathrm{E}}_{gg'}(\mathbf{q})|\chi_{g'}(t)\rangle\\ &= \tilde{S}^{\mathrm{elec}}_{\mathrm{pop}}(\mathbf{q}, t) + \tilde{S}^{\mathrm{elec}}_{\mathrm{coh}}(\mathbf{q}, t)\end{aligned} \tag{4}$$

where $\sum_{gg'}\rho_{g'g}(t)\langle\chi_g(t)|\hat{\sigma}^{\mathrm{E}}_{gg'}(\mathbf{q})|\chi_{g'}(t)\rangle$ is the time-evolving electronic charge density of the molecule in momentum space, $\tilde{S}^{\mathrm{elec}}_{\mathrm{pop}}(\mathbf{q}, t)$ is the electronic population (elastic) contribution, and $\tilde{S}^{\mathrm{elec}}_{\mathrm{coh}}(\mathbf{q}, t)$ is the electronic coherence (inelastic) contribution. The pure electronic coherence signal can be detected by varying the energy difference between the X-ray probe pulse and the reference pulse corresponding to the energy gap between the states of interest.

Unlike X-ray scattering that follows Thomson scattering dominated by the electronic charge density of the molecule, electron scattering follows Rutherford scattering and depends on the electrostatic Coulomb interaction of the traveling electrons with both electronic and nuclear charge density of the molecule.[39] The heterodyne-detected electron diffraction signal is thus given by

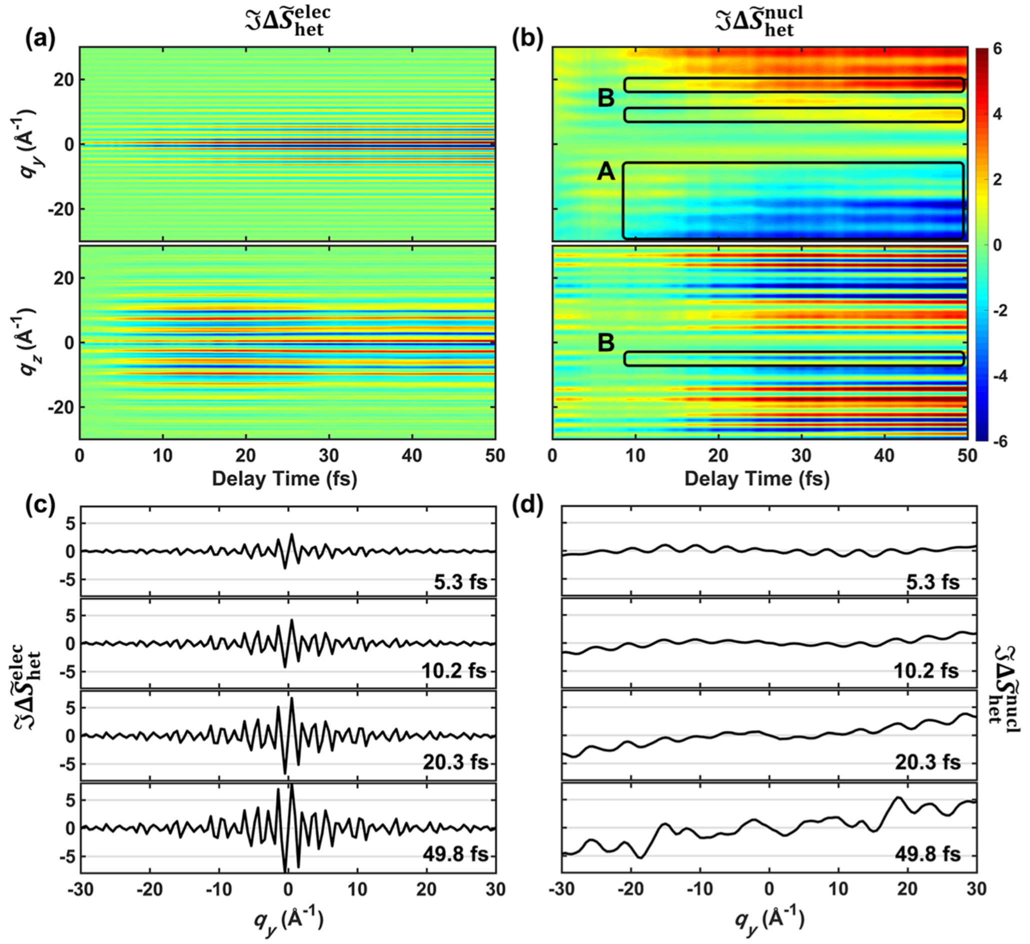

Figure 3. Simulated time-resolved difference diffraction signals from eq 5 for (a) electronic and (b) nuclear charge densities, respectively. The diffuse characters of the signals are marked by A, while the localized peaks are marked by B (all localized peaks are represented by B; here, only three of them are marked for clarity). Here, $\Delta\tilde{S}^{\mathrm{elec/nucl}}_{\mathrm{het}}(\mathbf{q}, T) = \tilde{S}^{\mathrm{elec/nucl}}_{\mathrm{het}}(\mathbf{q}, T) - \tilde{S}^{\mathrm{elec/nucl}}_{\mathrm{het}}(\mathbf{q}, T < 0)$. The signals are shown along q_y ($q_x = q_z = 0$) and q_z ($q_x = q_y = 0$), respectively. Vertical slices of (a,b) along q_y at characteristic times T are given in (c,d). See Figure 1 inset for the Cartesian coordinates.

$$\begin{aligned}\tilde{S}^{\mathrm{UED}}_{\mathrm{het}}(\mathbf{q}, t) &= \frac{1}{q^2}\left(\sum_{gg'} \rho_{g'g}(t)\langle\chi_g(t)|\hat{\sigma}^{\mathrm{E}}_{gg'}(\mathbf{q})|\chi_{g'}(t)\rangle\right.\\ &\quad \left.+ \sum_{g} \rho_{gg}(t)\langle\chi_g(t)|\hat{\sigma}^{\mathrm{N}}_{gg}(\mathbf{q})|\chi_g(t)\rangle\right)\\ &= \frac{1}{q^2}(\tilde{S}^{\mathrm{elec}}_{\mathrm{pop}}(\mathbf{q}, t) + \tilde{S}^{\mathrm{elec}}_{\mathrm{coh}}(\mathbf{q}, t) + \tilde{S}^{\mathrm{nucl}}_{\mathrm{pop}}(\mathbf{q}, t))\\ &= \frac{1}{q^2}(\tilde{S}^{\mathrm{elec}}_{\mathrm{het}}(\mathbf{q}, t) + \tilde{S}^{\mathrm{nucl}}_{\mathrm{het}}(\mathbf{q}, t))\end{aligned} \tag{5}$$

Here, $\hat{\sigma}^{\mathrm{N}}_{gg}(\mathbf{q})$ is the nuclear charge density operator, $\sum_g \rho_{gg}(t)\langle\chi_g(t)|\hat{\sigma}^{\mathrm{N}}_{gg}(\mathbf{q})|\chi_g(t)\rangle$ is the time-evolving nuclear charge density of the molecule in momentum space, $\tilde{S}^{\mathrm{nucl}}_{\mathrm{pop}}(\mathbf{q}, t)$ is the nuclear contribution to the diffraction signal, and $\tilde{S}^{\mathrm{elec}}_{\mathrm{het}}(\mathbf{q}, t) = \tilde{S}^{\mathrm{elec}}_{\mathrm{pop}}(\mathbf{q}, t) + \tilde{S}^{\mathrm{elec}}_{\mathrm{coh}}(\mathbf{q}, t)$. At the CIs, the motion of electrons and nuclei become strongly coupled through the nonadiabatic couplings in the effective Hamiltonian. However, this does not change the fact that the molecular response is expressed in terms of matrix elements of the nuclear and electronic charge density operators. While in homodyne-detected electron diffraction, there are cross-terms, $\sigma^{\mathrm{E}}(-\mathbf{q})\sigma^{\mathrm{N}}(\mathbf{q})$, which contain products of nuclear and electronic charge densities;[23] this is not the case in heterodyne-detected diffraction used here because it is linear in the charge densities ($\langle\hat{\sigma}(\mathbf{q}, t)\rangle$), whereas homodyne signals are quadratic ($\langle\hat{\sigma}(-\mathbf{q}, t)\hat{\sigma}(\mathbf{q}, t)\rangle$). Thus, the nuclear contribution can be isolated by the proposed measurement. Note that because X-ray diffraction is proportional to the Thomson cross section,[40] while electron diffraction is proportional to the Rutherford cross section,[41] careful normalization is required when combining the $S^{\mathrm{UED}}_{\mathrm{het}}$ and $S^{\mathrm{XRD}}_{\mathrm{het}}$ measurements since the diffraction signal strengths are directly related to their scattering cross sections.[42] This is crucial for the subtraction of X-ray and electron diffraction signals in order to isolate the nuclear contribution to the signal. Because $\hat{\sigma}^{\mathrm{E}}(\mathbf{q}) = \int \mathrm{d}\,\mathbf{r}\hat{\sigma}^{\mathrm{E}}(\mathbf{r})\, e^{i\mathbf{q}\cdot\mathbf{r}}$, it is equal to N_{el} when $\mathbf{q} = 0$ and converges to 0 at $\mathbf{q} \to \infty$. In eqs 4 and 5, we see that $\tilde{S}^{\mathrm{XRD}}_{\mathrm{het}}$ is proportional to the total number of electrons (N_{el}) in the molecule when $\mathbf{q} \to 0$ and converges to zero when $\mathbf{q} \to \infty$, while the $\tilde{S}^{\mathrm{UED}}_{\mathrm{het}}$ vanishes when $\mathbf{q} \to 0$ due to the opposite charge of electrons and nuclei cancels out. These intrinsic properties can be used to normalize the individual diffraction signals. Because the X-ray and electron pulse lengths could be slightly different, the diffraction signals should be deconvoluted with their respective instrument functions in the subtraction procedure.

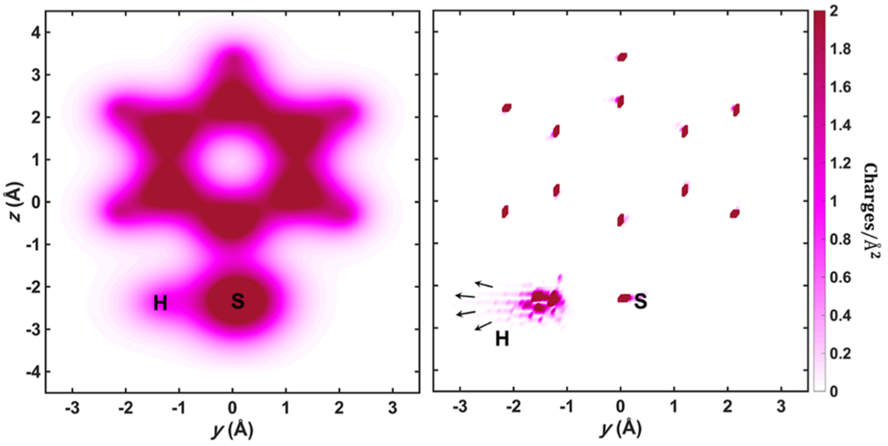

Figure 4. Real-space images of the total electronic (left) and nuclear (right) charge densities at $t = 5.3$ fs. The charge densities are presented in the $y-z$ plane by integrating over the x direction. Black arrows in the right panel mark the directions of the nuclear wave-packet momentum as the hydrogen atom dissociates. See Figure 1 inset for the Cartesian coordinates.

The independent atom model (IAM)[43] commonly used in crystallography for conventional (homodyne) X-ray and electron diffractions can be similarly extended to heterodyne-detected diffraction. Using tabulated atomic form factors $f_a(\mathbf{q})$, $\tilde{S}_{\mathrm{het}}^{\mathrm{XRD}}$ and $\tilde{S}_{\mathrm{het}}^{\mathrm{UED}}$ are then recast as

$$\tilde{S}_{\mathrm{het}}^{\mathrm{XRD}}(\mathbf{q}, t) = \sum_g \rho_{gg}(t) \int \mathrm{d}\,\mathbf{R} \chi_g^*(\mathbf{R}, t) \chi_g(\mathbf{R}, t) \sum_a |f_a(\mathbf{q})| \, \mathrm{e}^{i\mathbf{q}\cdot\mathbf{R}_a(\mathbf{R})} \tag{6}$$

$$\tilde{S}_{\mathrm{het}}^{\mathrm{UED}}(\mathbf{q}, t) = \frac{1}{q^2} \sum_g \rho_{gg}(t) \int \mathrm{d}\,\mathbf{R} \chi_g^*(\mathbf{R}, t) \chi_g(\mathbf{R}, t) \sum_a (Z_a - |f_a(\mathbf{q})|) \, \mathrm{e}^{i\mathbf{q}\cdot\mathbf{R}_a(\mathbf{R})} \tag{7}$$

where $\mathbf{R}_a(\mathbf{R})$ is the ath atom position for a given nuclear structure $\mathbf{R}$ and Z_a is the atomic number. The IAM approximates the electron density as a sum of atomic electron densities centered at the positions of the nuclei [*i.e.*, $\sigma^{\mathrm{E}}(\mathbf{q}) = \sum_a |f_a(\mathbf{q})| \, \mathrm{e}^{i\mathbf{q}\cdot\mathbf{R}_a(\mathbf{R})}$ and $\sigma^{\mathrm{N}}(\mathbf{q}) = \sum_a Z_a \, \mathrm{e}^{i\mathbf{q}\cdot\mathbf{R}_a(\mathbf{R})}$]. It provides an incomplete description of the electron density in molecules since it neglects chemical bonds and electronic excitations.[24,44] Comparing eqs 6 and 7 with eqs 4 and 5, we note that the IAM also neglects the electronic coherences when more than one electronic state is active. These effects must be taken into account when interpreting time-resolved diffraction experiments. We have used *ab initio* electronic charge densities and eqs 4 and 5 to simulate the diffraction signals so that the effects of chemical bonding, electronic excitation, and coherences are fully incorporated.

■ RESULTS AND DISCUSSION

The total (nuclear + electron) molecular wave function obtained by our dynamical simulations was used to compute the time-resolved heterodyne-detected X-ray and electron diffraction signals. In this section, we show theoretically that the nuclear part of the signal clearly tracks the evolution and dispersion of the nuclear wave packet, which is much less pronounced in the electronic signal. The purely electronic coherence terms originating from the passage thorough CIs can be separated out in the heterodyne-detected X-ray diffraction by energy-resolved detection. This is not possible by using X-ray homodyne diffraction due to the presence of mixed elastic−inelastic contributions.[45,46] Previous simulation studies of thiophenol have shown that stimulated X-ray Raman signals are also sensitive to electronic coherences during the CI dynamics but do not capture the evolution of the nuclear wave packet.[47,48] The present combination of two heterodyne diffraction measurements thus provides a complete picture of the nuclear wave packet, resulting in a real-space imaging of nuclear + electronic motions and their vibronic couplings during the passage through CIs.

Using the molecular wave-packet dynamics depicted in Figure 2, we have simulated the time-resolved heterodyne-detected X-ray and electron diffraction signals for an oriented gas-phase thiophenol (see Figure 1 inset). Both X-ray and electron diffraction from three-dimensionally aligned gas-phase molecules have been demonstrated experimentally,[49,50] indicating the feasibility of time-resolved diffraction of gas-phase molecules in the molecular frame.[27,51] Figure 3 shows the electronic $\tilde{S}_{\mathrm{het}}^{\mathrm{elec}}$ and the nuclear $\tilde{S}_{\mathrm{het}}^{\mathrm{nucl}}$ contributions to the diffraction signals. The former can be directly measured in X-ray diffraction, while the purely nuclear contribution is obtained by subtracting the X-ray and electron heterodyne diffraction given by eqs 4 and 5. The variation with q_y is dominated by the change along the S−H distance, and q_z mainly depends on the nuclear motion corresponding to the H−S−C angle. It is evident that the signal arising from the nuclear charge densities is much broader and spans a larger $\mathbf{q}$ regime, compared to the signal arising from electronic charge densities. This is because the nuclear charge densities are more localized in real space than the diffuse electronic densities, as illustrated in Figure 4. In the Fourier-conjugate $\mathbf{q}$ space, the nuclear contribution is thus more diffuse, while the electronic contribution exhibits rapidly oscillating features. In addition, because the total nuclear charge density is real, the imaginary part of its Fourier transform is an odd function resulting in inverted signs with respect to the origin in heterodyne signals. This feature can be used to calibrate the detector geometry and minimize experimental noise.

Both electronic and nuclear signals in Figure 3 contain time-dependent features that reflect the ~50 fs dissociation dynamics, as described in Figure 2. Figure 3a,c shows the electronic signals that are dominated by the rapid oscillatory features originating from the diffuse character of electronic charge densities in real space. Their rise over time reflects the

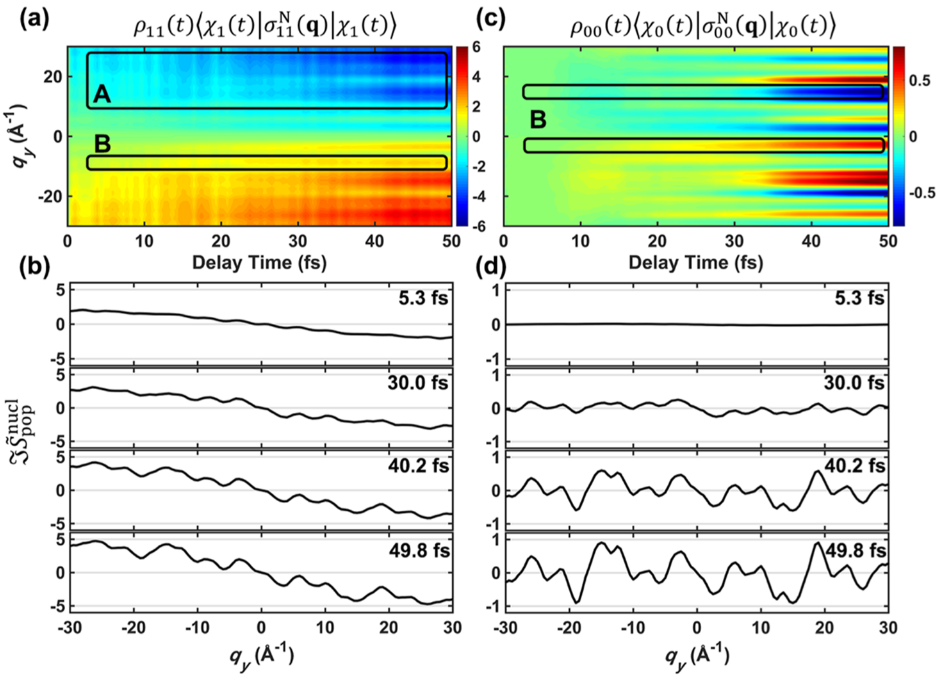

Figure 5. Population contribution to the diffraction signals. (a) $\mathcal{I}\tilde{S}^{\text{nucl}}_{\text{pop}}$ for the S_1 state and its vertical slices at characteristic times T are given in (b). (c) $\mathcal{I}\tilde{S}^{\text{nucl}}_{\text{pop}}$ for the S_0 state and its vertical slices at characteristic times T are given in (d). See Figure 1 inset for the Cartesian coordinates.

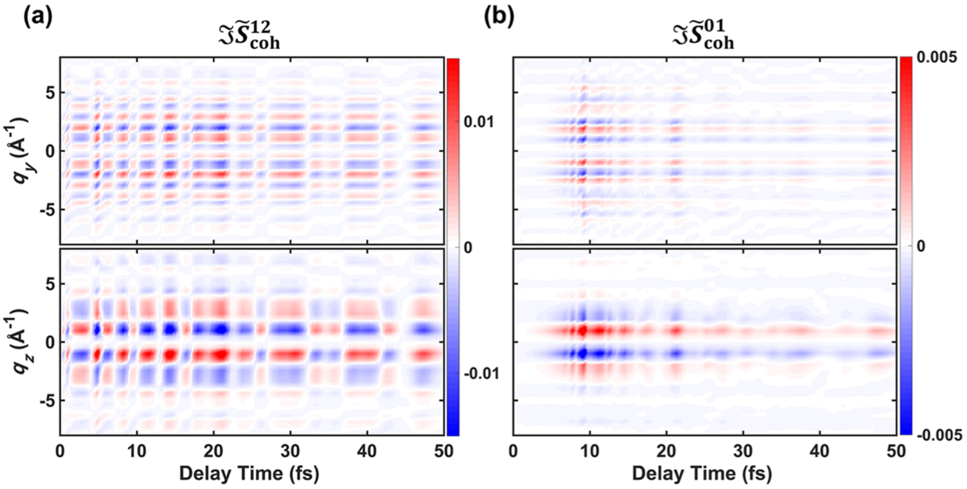

Figure 6. Contribution of coherences to the diffraction signals eq 4 for the (a) S_2/S_1 electronic coherence and (b) S_1/S_0 electronic coherence, respectively. See Figure 1 inset for the Cartesian coordinates.

change of electronic charge densities as the molecule dissociates. It is clear in Figure 4 that the nuclear wave-packet motions are better resolved in the nuclear signals since the nuclear charge densities are unmasked by the surrounding much more delocalized electron densities. Figure 3b,d reveals two distinct features of nuclear signals: an overall variation of the magnitude across a broad q regime marked A and localized peaks marked B. Recalling the inverse relation between real space and reciprocal space, one could immediately speculate that feature A is caused by some localized real space structures, while feature B originates from more diffuse patterns or structural changes at long distances such as bond dissociations. To further trace the origin of different features in the signals, we present in Figure 5 the population contributions of the nuclear term $\tilde{S}^{\text{nucl}}_{\text{pop}}$ to the overall diffraction signals for the S_1 and S_0 states (see the results of the electronic term $\tilde{S}^{\text{elecl}}_{\text{pop}}$ in Figure S1). Figure 5a,b shows mixed diffuse (A) and localized (B) nuclear signals along q_y for S_1, whereas panels 5c,d are dominated by the localized peaks (B) for S_0. In Figure 2, we see that the nuclear wave packet bifurcates after passing the S_2/S_1 CI, resulting in a partially localized nuclear wave packet near the Franck−Condon region (<1.5 Å) on the S_1 surface, whereas the other part of the nuclear wave packet spreads to a longer S−H distance. In contrast, on the S_0 surface, after passing the S_1/S_0 CI, the nuclear wave packet only moves to longer S−H distances, eventually leading to S−H bond breaking. Since there is only one dissociation pathway on the S_0 surface, the solely localized character (B) of the signals for S_0 in Figure 5c must come from the broad nuclear wave packet along the S−H dissociation channel, while the diffuse character

https://doi.org/10.1021/jacs.2c01311
J. Am. Chem. Soc. 2022, 144, 7796−7804

(A) of the signals that only appears in Figure 5a for the S_1 state corresponds to the partially localized nuclear wave packet near the Franck−Condon region. In addition, because the nuclear wave packet rapidly spreads along the H−S−C coordinate, the nuclear signals along q_z in Figure 3b are dominated by the localized peaks, reflecting the diffuse character of the wave packet along the H−S−C angle.

Armed with the knowledge of the origin of features A and B in the nuclear signals, we can now interpret the overall nuclear signals along q_y in Figure 3b,d by identifying and separately inspecting these two features. A very weak localized feature (B) before 10 fs indicates that a small portion of the nuclear wave packet undergoes a rapid dissociation, consistent with the dynamics depicted in Figure 2. The diffuse feature (A) shows up at ∼10 fs, then gradually broadens, and persists after ∼20 fs. The localized feature (B) rises steeply after 10 fs and reaches a plateau after ∼40 fs. This unambiguously shows that a major portion of the nuclear wave packet reaches the S_2/S_1 CI within 10 fs and then bifurcates into two pathways, as is evident from the appearance of both features (A and B) in the nuclear signals after ∼10 fs. The different timescales of A and B indicate that one portion of the nuclear wave packet approaches the Franck−Condon region and localizes on the S_1 surface at around 20 fs (based on feature A persisting after ∼20 fs), while the other part continues to pass the S_1/S_0 CI, leading to hydrogen dissociation within 40 fs (based on feature B reaching a plateau after ∼40 fs). The evolution and bifurcation of the nuclear wave packet can be directly revealed by the nuclear signals, while the overall similarity of the electronic signals (see Figures 3 and S1) prevents a direct access to these subtle details as they are largely blurred by the much more diffuse electron densities (see Figure S2).

The nuclear contribution $\tilde{S}_{\text{pop}}^{\text{nucl}}$ is more sensitive to the trajectory and shape of the nuclear wave packet but carries no information on the electronic coherences created as the nuclear wave packet passes through the CI. This information contained in the electronic coherence contribution $\tilde{S}_{\text{coh}}^{\text{elec}}$ shown in Figure 6 can be isolated from the heterodyne-detected X-ray diffraction by frequency-resolved detection. As can be seen in eq 4, in heterodyne X-ray diffraction, the elastic scattering is responsible for the population dynamics, while the inelastic scattering solely arises from the electronic coherences as previously described.[36] The S_2/S_1 electronic coherence signal in Figure 6a appears right after time zero, whereas the S_1/S_0 electronic coherence signal in Figure 6b starts a bit later at around 5 fs and peaks at ∼10 fs. The initially excited molecule thus approaches the S_2/S_1 CI very rapidly and starts to relax to S_1. At around 10 fs, the nuclear wave packet reaches the S_1/S_0 CI and then gradually transfers to S_0. This is consistent with the observation that the S_0 signal in Figure 5c,d is very weak before 10 fs and starts to rise after 20 fs, while the S_1 signal in Figure 5a,b emerges much earlier. The periodic beating of the electronic coherence signal is induced by the transient vibronic coherences generated near CI, which also features in stimulated ultrafast X-ray Raman signals.[52,53]

■ CONCLUSIONS

Ultrafast X-ray and electron diffraction are complementary techniques for monitoring transient molecular structures. Comparisons of the two techniques have been discussed extensively.[23,42,54,55] Even though X-ray diffraction has a much smaller cross section and covers a smaller regime of scattering angles, the high flux and energy of free electron laser X-ray pulses make up for these shortcomings.[56,57] The relativistic megaelectron volt electron pulses[58,59] with advanced time-sorting methods[60,61] largely overcome the space-charge effects, making femtosecond-resolved electron diffraction signals comparable to X-ray diffraction. We have simulated diffraction signals over a broad range of scattering vectors (q up to 30 Å^{-1}). In practice, the nuclear signal is limited by the relatively short momentum ranges of the X-ray diffraction signals. The ongoing high energy upgrade of Linac Coherent Light Source (LCLS-II-HE) could provide q ranges up to 14 Å^{-1}, which is adequate for observing distinct features of nuclear signals, as discussed in this study. Our proposed experiment requires heterodyne detection of both X-ray and electron diffraction. This can be achieved by either exploiting the interreference pattern between the studied sample and a known reference sample[62,63] or by introducing a second coincident reference pulse with a controlled relative phase.[36,64] Here, we have employed the latter, but the concept is equally applicable to the former.

We have shown that the nuclear wave packet evolution can be directly imaged by combining ultrafast X-ray and electron heterodyne diffraction. We have shown how the signals from nuclear and electronic charge densities during the photodissociation dynamics of thiophenol can be sorted out. This results in a detailed imaging of the shape and trajectory of the nuclear wave packet, as well as the electronic coherences in the vicinity of the CIs. We note that the studied hydrogen dissociation dynamics in thiophenol is mainly a single-electron/nucleus effect occurring on top of a background of 58 electrons/nuclei. The observation of the effects from a single electron has been demonstrated in both homodyne X-ray and electron diffraction experiments,[24,44] where their desired relative signal changes are proportional to $1/N_{\text{el}}^2$. Because heterodyne-detected diffraction signals are linear in the charge densities, the relative signal changes proportional to the $1/N_{\text{el}}$ increase dramatically. This indicates that the required signal-to-noise ratio is feasible and may be even superior under the right experimental conditions.

The proposed measurement is very challenging and requires extensive works for its experimental realization. Our results show that it is worth the effort as it provides a promising direction for the direct imaging of nuclear wave packets. An intensive world-wide effort is being made in the development of X-ray free-electron laser machines and relativistic mega-electron volt electron sources and the necessary theoretical methods. Our study demonstrates that these high-risk/high-gain experiments could reveal chemical information unavailable otherwise.

■ ASSOCIATED CONTENT

SI Supporting Information

The Supporting Information is available free of charge at https://pubs.acs.org/doi/10.1021/jacs.2c01311.

> *Ab initio* quantum chemistry, electronic and nuclear charge densities, wave-packet simulations, population contribution to the electronic signals, and real-space electronic/nuclear charge densities (PDF)

■ AUTHOR INFORMATION

Corresponding Authors

Haiwang Yong − *Department of Chemistry, University of California, Irvine, Irvine, California 92697, United States;*

Department of Physics and Astronomy, University of California, Irvine, Irvine, California 92697, United States; orcid.org/0000-0002-5860-4259; Email: h.yong@uci.edu

Shaul Mukamel − *Department of Chemistry, University of California, Irvine, Irvine, California 92697, United States; Department of Physics and Astronomy, University of California, Irvine, Irvine, California 92697, United States;* orcid.org/0000-0002-6015-3135; Email: smukamel@uci.edu

Author

Daniel Keefer − *Department of Chemistry, University of California, Irvine, Irvine, California 92697, United States; Department of Physics and Astronomy, University of California, Irvine, Irvine, California 92697, United States;* orcid.org/0000-0001-5941-5567

Complete contact information is available at: https://pubs.acs.org/10.1021/jacs.2c01311

Notes

The authors declare no competing financial interest.

ACKNOWLEDGMENTS

The support of the Chemical Sciences, Geosciences, and Biosciences Division, Office of Basic Energy Sciences, Office of Science, U.S. Department of Energy through award no. DE-FG02-04ER15571 is gratefully acknowledged. D.K. gratefully acknowledges support from the Alexander von Humboldt Foundation through the Feodor Lynen Program. We thank Markus Kowalewski for providing the QDng quantum dynamics code.

REFERENCES

(1) Garraway, B. M.; Suominen, K.-A. Wave Packet Dynamics in Molecules. *Contemp. Phys.* **2002**, *43*, 97−114.

(2) Worth, G. A.; Cederbaum, L. S. Beyond Born-Oppenheimer: Molecular Dynamics Through a Conical Intersection. *Annu. Rev. Phys. Chem.* **2004**, *55*, 127−158.

(3) Bircher, M. P.; Liberatore, E.; Browning, N. J.; Brickel, S.; Hofmann, C.; Patoz, A.; Unke, O. T.; Zimmermann, T.; Chergui, M.; Hamm, P.; et al. Nonadiabatic Effects in Electronic and Nuclear Dynamics. *Struct. Dyn.* **2017**, *4*, 061510.

(4) Schuurman, M. S.; Stolow, A. Dynamics at Conical Intersections. *Annu. Rev. Phys. Chem.* **2018**, *69*, 427−450.

(5) Zewail, A. H. Femtochemistry: Atomic-Scale Dynamics of the Chemical Bond Using Ultrafast Lasers (Nobel Lecture). *Angew. Chem., Int. Ed.* **2000**, *39*, 2586−2631.

(6) Rafiq, S.; Scholes, G. D. From Fundamental Theories to Quantum Coherences in Electron Transfer. *J. Am. Chem. Soc.* **2019**, *141*, 708−722.

(7) Li, Z.; Gyawali, S.; Ischenko, A. A.; Hayes, S.; Miller, R. J. D. Mapping Atomic Motions with Electrons: Toward the Quantum Limit to Imaging Chemistry. *ACS Photonics* **2020**, *7*, 296−320.

(8) Kim, J. G.; Choi, E. H.; Lee, Y.; Ihee, H. Femtosecond X-ray Liquidography Visualizes Wavepacket Trajectories in Multidimensional Nuclear Coordinates for a Bimolecular Reaction. *Acc. Chem. Res.* **2021**, *54*, 1685−1698.

(9) Isnard, O. A Review of in Situ and/or Time Resolved Neutron Scattering. *C. R. Phys.* **2007**, *8*, 789−805.

(10) Pieper, J. Time-Resolved Quasielastic Neutron Scattering Studies of Native Photosystems. *Biochim. Biophys. Acta* **2010**, *1804*, 83−88.

(11) Pomerantz, I.; McCary, E.; Meadows, A. R.; Arefiev, A.; Bernstein, A. C.; Chester, C.; Cortez, J.; Donovan, M. E.; Dyer, G.; Gaul, E. W.; et al. Ultrashort Pulsed Neutron Source. *Phys. Rev. Lett.* **2014**, *113*, 184801.

(12) Dudek, R. C.; Weber, P. M. Ultrafast Diffraction Imaging of the Electrocyclic Ring-Opening Reaction of 1,3-Cyclohexadiene. *J. Phys. Chem. A* **2001**, *105*, 4167−4171.

(13) Ruan, C.-Y.; Lobastov, V. A.; Srinivasan, R.; Goodson, B. M.; Ihee, H.; Zewail, A. H. Ultrafast Diffraction and Structural Dynamics: The Nature of Complex Molecules Far From Equilibrium. *Proc. Natl. Acad. Sci. U.S.A.* **2001**, *98*, 7117−7122.

(14) Biasin, E.; van Driel, T. B.; Kjær, K. S.; Dohn, A. O.; Christensen, M.; Harlang, T.; Vester, P.; Chabera, P.; Liu, Y.; Uhlig, J.; et al. Femtosecond X-ray Scattering Study of Ultrafast Photoinduced Structural Dynamics in Solvated $[\mathrm{Co(terpy)_2}]^{2+}$. *Phys. Rev. Lett.* **2016**, *117*, 013002.

(15) Yang, J.; Guehr, M.; Shen, X.; Li, R.; Vecchione, T.; Coffee, R.; Corbett, J.; Fry, A.; Hartmann, N.; Hast, C.; et al. Diffractive Imaging of Coherent Nuclear Motion in Isolated Molecules. *Phys. Rev. Lett.* **2016**, *117*, 153002.

(16) Ischenko, A. A.; Weber, P. M.; Miller, R. J. D. Capturing Chemistry in Action with Electrons: Realization of Atomically Resolved Reaction Dynamics. *Chem. Rev.* **2017**, *117*, 11066−11124.

(17) Stankus, B.; Yong, H.; Zotev, N.; Ruddock, J. M.; Bellshaw, D.; Lane, T. J.; Liang, M.; Boutet, S.; Carbajo, S.; Robinson, J. S.; et al. Ultrafast X-Ray Scattering Reveals Vibrational Coherence Following Rydberg Excitation. *Nat. Chem.* **2019**, *11*, 716−721.

(18) Ware, M. R.; Glownia, J. M.; Al-Sayyad, N.; O'Neal, J. T.; Bucksbaum, P. H. Characterizing Dissociative Motion in Time-Resolved X-Ray Scattering From Gas-Phase Diatomic Molecules. *Phys. Rev. A* **2019**, *100*, 033413.

(19) Kim, J. G.; Nozawa, S.; Kim, H.; Choi, E. H.; Sato, T.; Kim, T. W.; Kim, K. H.; Ki, H.; Kim, J.; Choi, M.; et al. Mapping the Emergence of Molecular Vibrations Mediating Bond Formation. *Nature* **2020**, *582*, 520−524.

(20) Kunnus, K.; Vacher, M.; Harlang, T. C. B.; Kjær, K. S.; Haldrup, K.; Biasin, E.; van Driel, T. B.; Pápai, M.; Chabera, P.; Liu, Y.; et al. Vibrational Wavepacket Dynamics in Fe Carbene Photosensitizer Determined with Femtosecond X-Ray Emission and Scattering. *Nat. Commun.* **2020**, *11*, 634.

(21) Kirrander, A.; Weber, P. Fundamental Limits on Spatial Resolution in Ultrafast X-Ray Diffraction. *Appl. Sci.* **2017**, *7*, 534.

(22) Keefer, D.; Aleotti, F.; Rouxel, J. R.; Segatta, F.; Gu, B.; Nenov, A.; Garavelli, M.; Mukamel, S. Imaging Conical Intersection Dynamics during Azobenzene Photoisomerization by Ultrafast X-ray Diffraction. *Proc. Natl. Acad. Sci. U.S.A.* **2021**, *118*, No. e2022037118.

(23) Rouxel, J. R.; Keefer, D.; Mukamel, S. Signatures of Electronic and Nuclear Coherences in Ultrafast Molecular X-Ray and Electron Diffraction. *Struct. Dyn.* **2021**, *8*, 014101.

(24) Yang, J.; Zhu, X.; Nunes, J. P. F.; Yu, J. K.; Parrish, R. M.; Wolf, T. J. A.; Centurion, M.; Gühr, M.; Li, R.; Liu, Y.; et al. Simultaneous Observation of Nuclear and Electronic Dynamics by Ultrafast Electron Diffraction. *Science* **2020**, *368*, 885−889.

(25) Tegze, M.; Faigel, G. X-ray Holography with Atomic Resolution. *Nature* **1996**, *380*, 49−51.

(26) Marchesini, S.; Boutet, S.; Sakdinawat, A. E.; Bogan, M. J.; Bajt, S.; Barty, A.; Chapman, H. N.; Frank, M.; Hau-Riege, S. P.; Szöke, A.; et al. Massively Parallel X-Ray Holography. *Nat. Photonics* **2008**, *2*, 560−563.

(27) Barty, A.; Küpper, J.; Chapman, H. N. Molecular Imaging Using X-Ray Free-Electron Lasers. *Annu. Rev. Phys. Chem.* **2013**, *64*, 415−435.

(28) King, W. E.; Campbell, G. H.; Frank, A.; Reed, B.; Schmerge, J. F.; Siwick, B. J.; Stuart, B. C.; Weber, P. M. Ultrafast Electron Microscopy in Materials Science, Biology, and Chemistry. *J. Appl. Phys.* **2005**, *97*, 111101.

(29) Feist, A.; Bach, N.; Rubiano da Silva, N.; Danz, T.; Möller, M.; Priebe, K. E.; Domröse, T.; Gatzmann, J. G.; Rost, S.; Schauss, J.; et al. Ultrafast Transmission Electron Microscopy Using a Laser-Driven Field Emitter: Femtosecond Resolution with a High Coherence Electron Beam. *Ultramicroscopy* **2017**, *176*, 63−73.

(30) Lim, I. S.; Lim, J. S.; Lee, Y. S.; Kim, S. K. Experimental and Theoretical Study of the Photodissociation Reaction of Thiophenol at 243 nm: Intramolecular Orbital Alignment of the Phenylthiyl Radical. *J. Chem. Phys.* **2007**, *126*, 034306.

(31) Ashfold, M. N. R.; Devine, A. L.; Dixon, R. N.; King, G. A.; Nix, M. G. D.; Oliver, T. A. A. Exploring Nuclear Motion Through Conical Intersections in the UV Photodissociation of Phenols and Thiophenol. *Proc. Natl. Acad. Sci. U.S.A.* **2008**, *105*, 12701−12706.

(32) You, H. S.; Han, S.; Lim, J. S.; Kim, S. K. ($\pi\pi^*/\pi\sigma^*$) Conical Intersection Seam Experimentally Observed in the S-D Bond Dissociation Reaction of Thiophenol-D_1. *J. Phys. Chem. Lett.* **2015**, *6*, 3202−3208.

(33) Wang, L.; Akimov, A.; Prezhdo, O. V. Recent Progress in Surface Hopping: 2011-2015. *J. Phys. Chem. Lett.* **2016**, *7*, 2100−2112.

(34) Curchod, B. F. E.; Martínez, T. J. Ab Initio Nonadiabatic Quantum Molecular Dynamics. *Chem. Rev.* **2018**, *118*, 3305−3336.

(35) Nelson, T. R.; White, A. J.; Bjorgaard, J. A.; Sifain, A. E.; Zhang, Y.; Nebgen, B.; Fernandez-Alberti, S.; Mozyrsky, D.; Roitberg, A. E.; Tretiak, S. Non-adiabatic Excited-State Molecular Dynamics: Theory and Applications for Modeling Photophysics in Extended Molecular Materials. *Chem. Rev.* **2020**, *120*, 2215−2287.

(36) Rouxel, J. R.; Kowalewski, M.; Bennett, K.; Mukamel, S. X-ray Sum Frequency Diffraction for Direct Imaging of Ultrafast Electron Dynamics. *Phys. Rev. Lett.* **2018**, *120*, 243902.

(37) Huang, S.; Ding, Y.; Feng, Y.; Hemsing, E.; Huang, Z.; Krzywinski, J.; Lutman, A. A.; Marinelli, A.; Maxwell, T. J.; Zhu, D. Generating Single-Spike Hard X-Ray Pulses with Nonlinear Bunch Compression in Free-Electron Lasers. *Phys. Rev. Lett.* **2017**, *119*, 154801.

(38) Li, C.; Wang, W.; Zhang, H.; Guo, Z.; Jiang, S.; He, Z.; Zhang, S.; Jia, Q.; Wang, L.; He, D. Relativistic Attosecond Electron Pulses from a Photocathode Radio-Frequency Gun. *Phys. Rev. Appl.* **2021**, *16*, 054007.

(39) Thakkar, A. J.; Tripathi, A. N.; Smith, V. H. Molecular X-ray- and Electron-Scattering Intensities. *Phys. Rev. A: At., Mol., Opt. Phys.* **1984**, *29*, 1108−1113.

(40) Warren, B. E. *X-ray Diffraction*; Addison-Wesley Publishing Company: Reading, MA, 1969.

(41) Hofstadter, R. Electron Scattering and Nuclear Structure. *Rev. Mod. Phys.* **1956**, *28*, 214−254.

(42) Ma, L.; Yong, H.; Geiser, J. D.; Moreno Carrascosa, A.; Goff, N.; Weber, P. M. Ultrafast X-ray and Electron Scattering of Free Molecules: A Comparative Evaluation. *Struct. Dyn.* **2020**, *7*, 034102.

(43) Debye, P. Zerstreuung Von Röenstrahlen. *Ann. Phys.* **1915**, *351*, 809−823.

(44) Yong, H.; Zotev, N.; Ruddock, J. M.; Stankus, B.; Simmermacher, M.; Carrascosa, A. M.; Du, W.; Goff, N.; Chang, Y.; Bellshaw, D.; et al. Observation of the Molecular Response to Light upon Photoexcitation. *Nat. Commun.* **2020**, *11*, 2157.

(45) Bennett, K.; Kowalewski, M.; Rouxel, J. R.; Mukamel, S. Monitoring Molecular Nonadiabatic Dynamics with Femtosecond X-Ray Diffraction. *Proc. Natl. Acad. Sci. U.S.A.* **2018**, *115*, 6538−6547.

(46) Simmermacher, M.; Moreno Carrascosa, A.; Henriksen, N. E.; Møller, K. B.; Kirrander, A. Theory of Ultrafast X-Ray Scattering by Molecules in the Gas Phase. *J. Chem. Phys.* **2019**, *151*, 174302.

(47) Cho, D.; Mukamel, S. Stimulated X-ray Raman Imaging of Conical Intersections. *J. Phys. Chem. Lett.* **2020**, *11*, 33−39.

(48) Cho, D.; Rouxel, J. R.; Mukamel, S. Stimulated X-ray Resonant Raman Spectroscopy of Conical Intersections in Thiophenol. *J. Phys. Chem. Lett.* **2020**, *11*, 4292−4297.

(49) Yang, J.; Beck, J.; Uiterwaal, C. J.; Centurion, M. Imaging of alignment and structural changes of carbon disulfide molecules using ultrafast electron diffraction. *Nat. Commun.* **2015**, *6*, 8172.

(50) Kierspel, T.; Morgan, A.; Wiese, J.; Mullins, T.; Aquila, A.; Barty, A.; Bean, R.; Boll, R.; Boutet, S.; Bucksbaum, P.; et al. X-ray Diffractive Imaging of Controlled Gas-Phase Molecules: Toward Imaging of Dynamics in the Molecular Frame. *J. Chem. Phys.* **2020**, *152*, 084307.

(51) Filsinger, F.; Meijer, G.; Stapelfeldt, H.; Chapman, H. N.; Küpper, J. State- and Conformer-Selected Beams of Aligned and Oriented Molecules for Ultrafast Diffraction Studies. *Phys. Chem. Chem. Phys.* **2011**, *13*, 2076−2087.

(52) Kowalewski, M.; Bennett, K.; Dorfman, K. E.; Mukamel, S. Catching Conical Intersections In the Act: Monitoring Transient Electronic Coherences by Attosecond Stimulated X-ray Raman Signals. *Phys. Rev. Lett.* **2015**, *115*, 193003.

(53) Keefer, D.; Schnappinger, T.; de Vivie-Riedle, R.; Mukamel, S. Visualizing Conical Intersection Passages via Vibronic Coherence Maps Generated by Stimulated Ultrafast X-ray Raman Signals. *Proc. Natl. Acad. Sci. U.S.A.* **2020**, *117*, 24069−24075.

(54) Spence, J. C. H. Outrunning Damage: Electrons vs X-rays-Timescales and Mechanisms. *Struct. Dyn.* **2017**, *4*, 044027.

(55) Stefanou, M.; Saita, K.; Shalashilin, D. V.; Kirrander, A. Comparison of Ultrafast Electron and X-ray Diffraction—A Computational Study. *Chem. Phys. Lett.* **2017**, *683*, 300−305.

(56) Emma, P.; Akre, R.; Arthur, J.; Bionta, R.; Bostedt, C.; Bozek, J.; Brachmann, A.; Bucksbaum, P.; Coffee, R.; Decker, F.-J.; et al. First Lasing and Operation of An Ångstrom-Wavelength Free-Electron Laser. *Nat. Photonics* **2010**, *4*, 641−647.

(57) Decking, W.; Abeghyan, S.; Abramian, P.; Abramsky, A.; Aguirre, A.; Albrecht, C.; Alou, P.; Altarelli, M.; Altmann, P.; Amyan, K.; et al. A MHz-Repetition-Rate Hard X-Ray Free-Electron Laser Driven by a Superconducting Linear Accelerator. *Nat. Photonics* **2020**, *14*, 391−397.

(58) Weathersby, S. P.; Brown, G.; Centurion, M.; Chase, T. F.; Coffee, R.; Corbett, J.; Eichner, J. P.; Frisch, J. C.; Fry, A. R.; Gühr, M.; et al. Mega-Electron-Volt Ultrafast Electron Diffraction at SLAC National Accelerator Laboratory. *Rev. Sci. Instrum.* **2015**, *86*, 073702.

(59) Qi, F.; Ma, Z.; Zhao, L.; Cheng, Y.; Jiang, W.; Lu, C.; Jiang, T.; Qian, D.; Wang, Z.; Zhang, W.; et al. Breaking 50 Femtosecond Resolution Barrier in MeV Ultrafast Electron Diffraction with a Double Bend Achromat Compressor. *Phys. Rev. Lett.* **2020**, *124*, 134803.

(60) Zhao, L.; Wu, J.; Wang, Z.; Tang, H.; Zou, X.; Jiang, T.; Zhu, P.; Xiang, D.; Zhang, J. Noninvasive Time-Sorting in Radio Frequency-Compressed Ultrafast Electron Diffraction. *Struct. Dyn.* **2021**, *8*, 044303.

(61) Shin, J.; Kim, H. W.; Baek, I. H.; Park, S.; Bark, H. S.; Oang, K. Y.; Jang, K. H.; Lee, K.; Rotermund, F.; Jeong, Y. U.; et al. Sub-10-fs Timing for Ultrafast Electron Diffraction with THz-Driven Streak Camera. *Laser Photonics Rev.* **2021**, *15*, 2000326.

(62) Woerner, M.; Zamponi, F.; Ansari, Z.; Dreyer, J.; Freyer, B.; Prémont-Schwarz, M.; Elsaesser, T. Concerted Electron and Proton Transfer in Ionic Crystals Mapped by Femtosecond X-Ray Powder Diffraction. *J. Chem. Phys.* **2010**, *133*, 064509.

(63) Zamponi, F.; Rothhardt, P.; Stingl, J.; Woerner, M.; Elsaesser, T. Ultrafast Large-Amplitude Relocation of Electronic Charge in Ionic Crystals. *Proc. Natl. Acad. Sci. U.S.A.* **2012**, *109*, 5207−5212.

(64) Cho, D.; Rouxel, J. R.; Kowalewski, M.; Lee, J. Y.; Mukamel, S. Attosecond X-Ray Diffraction Triggered by Core or Valence Ionization of a Dipeptide. *J. Chem. Theory Comput.* **2018**, *14*, 329−338.

Supporting Information:
Imaging Purely-Nuclear Quantum Dynamics in Molecules by Combined X-Ray and Electron Diffraction

Haiwang Yong*, Daniel Keefer, Shaul Mukamel*

Department of Chemistry, University of California, Irvine, California 92697, United States

Department of Physics and Astronomy, University of California, Irvine, California 92697, United States

* Correspondence to: smukamel@uci.edu (S. M.) and h.yong@uci.edu (H. Y.)

Ab initio quantum chemistry

The planar geometry of neutral ground state thiophenol was optimized using the SA4-CAS(12,11)/6-311++G(d,p) method. Consistent with previous study, the planar structure is more stable compared to the one with S-H bond perpendicular to the benzene plane.[1] The active space comprises 12 electrons in 11 orbitals (including three pairs of π/π* orbitals of the benzene ring, a nonbonding p-orbital of sulfur, and $\sigma_{\text{S-H}}$, $\sigma^*{}_{\text{S-H}}$, $\sigma_{\text{C-S}}$ and $\sigma^*{}_{\text{C-S}}$ orbitals), which has been found necessary for describing the photodissociation of the S-H bond.[2] Potential energy surfaces of the S_2, S_1 and S_0 adiabatic electronic states and the nonadiabatic coupling matrix elements of S_2/S_1 and S_1/S_0 were calculated at the same level of theory, by displacing the molecular structure along the two reactive coordinates. The complete active space self-consistent field (CASSCF) calculations were carried out using the Molpro electronic structure software package[3,4].

The electronic and nuclear densities

Using the ab initio calculations, both electronic and nuclear charge densities were evaluated in 0.05 Å increments in the S-H distance and 5° increments in the H-S-C angle. The electronic charge densities and transition charge densities in **q**-space (reciprocal space) were evaluated from the state specific charge density matrices, $P_{rs}^{gg'}$, according to

$$\sigma_{gg'}^{\mathrm{E}}(\mathbf{q},\mathbf{R}) = \int \mathrm{d}\mathbf{r} e^{i\mathbf{q}\cdot\mathbf{r}} \sigma_{gg'}^{\mathrm{E}}(\mathbf{r},\mathbf{R}) = \int \mathrm{d}\mathbf{r} e^{i\mathbf{q}\cdot\mathbf{r}} \sum_{rs} P_{rs}^{gg'}(\mathbf{R}) \phi_r(\mathbf{r},\mathbf{R}) \phi_s^*(\mathbf{r},\mathbf{R}), \qquad \text{(S1)}$$

where $\phi_r(\mathbf{r},\mathbf{R})$ is an atomic basis function for the r_{th} atomic orbital, g and g' are labels for electronic states, **r** and **R** are the electronic and nuclear coordinates. The grid-based $\sigma_{gg'}(\mathbf{r},\mathbf{R})$ in real space was calculated from the charge density matrices using PySCF software[5,6]. The nuclear charge density in **q**-space for a given nuclear structure **R** was calculated as

$$\sigma^{\mathrm{N}}(\mathbf{q},\mathbf{R}) = \sum_a Z_a e^{i\mathbf{q}\cdot\mathbf{R}_a(\mathbf{R})} \qquad \text{(S2)}$$

where a labels the a_{th} atom with atomic number Z_a at position $\mathbf{R}_{\boldsymbol{a}}(\mathbf{R})$. A derivation of heterodyne detected diffraction signals in the minimal coupling Hamiltonian picture was given earlier[7].

Wavepacket simulations

The photoinduced S-H bond cleavage in Thiophenol is simulated using exact nuclear wavepackets.[8] For the two reactive nuclear degrees of freedom with the first one being the S-H bond distance, and the second being the H-S-C angle (see Fig. 1 in the main text). Potential energy surfaces and related molecular quantities in this two-dimensional space are calculated with ab-initio quantum chemistry and subsequently discretized on a numerical grid with 1024 grid points in S-H and 256 grid points in H-S-C.

The effective Hamiltonian in matrix form comprising three electronic states a (S_0), b (S_1) and c (S_2) is given by

$$\hat{H} = \begin{pmatrix} \hat{T} + \hat{V}_a(\mathbf{R}) & \hat{K}_{ab} & 0 \\ \hat{K}_{ba} & \hat{T} + \hat{V}_b(\mathbf{R}) & \hat{K}_{bc} \\ 0 & \hat{K}_{cb} & \hat{T} + \hat{V}_c(\mathbf{R}) \end{pmatrix} \tag{S3}$$

where $\hat{V}$ are the potential energy surfaces. The kinetic energy operator $\hat{T}$ in Eq. S3 is given in the G-Matrix formalism[9],[10] according to

$$\hat{T} \backsimeq -\frac{\hbar^2}{2m}\sum_{o=1}^{2}\sum_{p=1}^{2}\frac{\partial}{\partial q_o}\left[G_{op}\frac{\partial}{\partial q_p}\right] \tag{S4}$$

with $o, p \in \mathbf{R}$ and the G-Matrix computed via its inverse elements

$$(G^{-1})_{op} = \sum_{i=1}^{3N} m_i \frac{\partial x_i}{\partial q_o}\frac{\partial x_i}{\partial q_p} \tag{S5}$$

$\widehat{K}_{gg'}$ in Eq. S3 approximate the nonadiabatic couplings between the electronic states g and g' and are given by[8]

$$\widehat{K}_{gg'} = \frac{1}{2m}\left(2f_{gg'}\frac{\partial}{\partial \mathbf{R}} + \frac{\partial}{\partial \mathbf{R}}f_{gg'}\right) \tag{S6}$$

with $f_{gg'}$ containing terms $\left\langle \Phi_g \middle| \frac{\partial}{\partial \mathbf{R}} \Phi_{g'} \right\rangle$ with the electronic wavefunction Φ. Since there is no conical intersection between S_0 and S_2, the electronic coupling between the electronic states a and c is negligible ($\widehat{K}_{ac} = 0$). The nuclear wavefunction $\chi(\mathbf{R}, t)$ is obtained by propagating the S_0 ground state vibrational wavefunction $\chi(\mathbf{R}, t_0)$ after impulsive excitation to S_2 with a Chebychev[11] scheme using 0.05 fs time step. A Butterworth filter[12] absorbs the wavepacket at S-H = 10 Å in all three states, as the photodissociation is completed. All terms in the diffraction signals were evaluated every 0.5 fs.

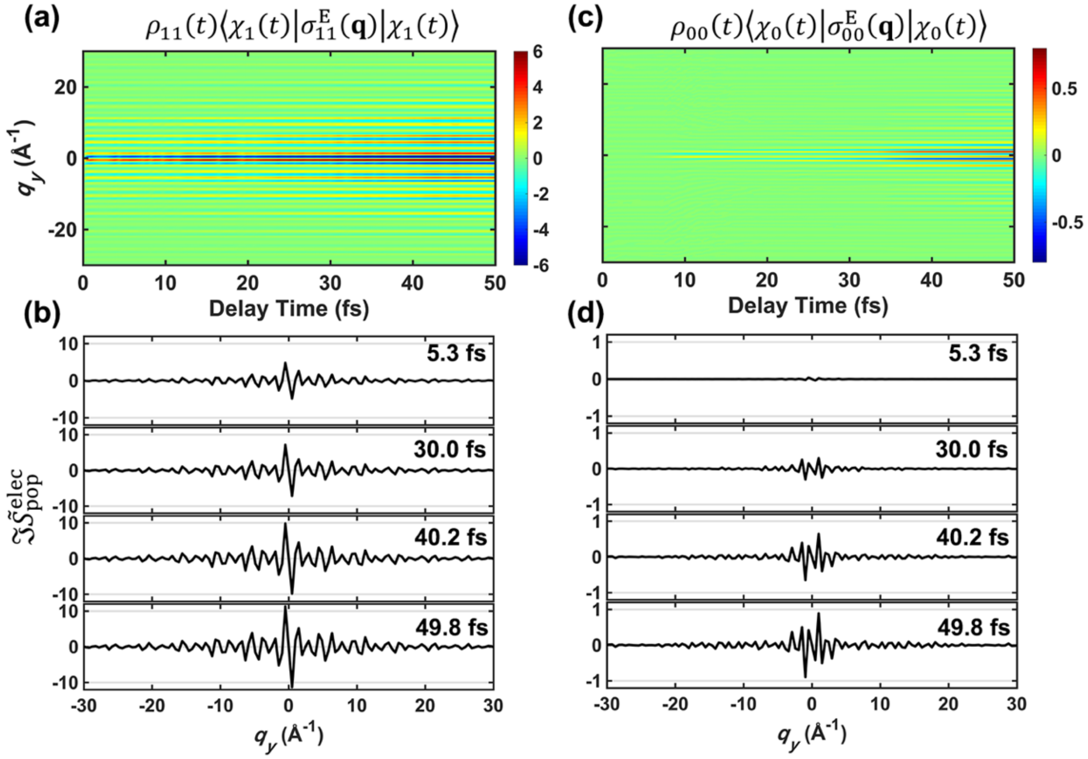

Figure S1. Population contribution to the diffraction signals. (a) $\Im\tilde{S}_{\mathrm{pop}}^{\mathrm{elec}}$ for the S$_1$ state and its vertical slices at characteristic times *T* are given in (b). (c) $\Im\tilde{S}_{\mathrm{pop}}^{\mathrm{elec}}$ for the S$_0$ state and its vertical slices at characteristic times *T* are given in (d).

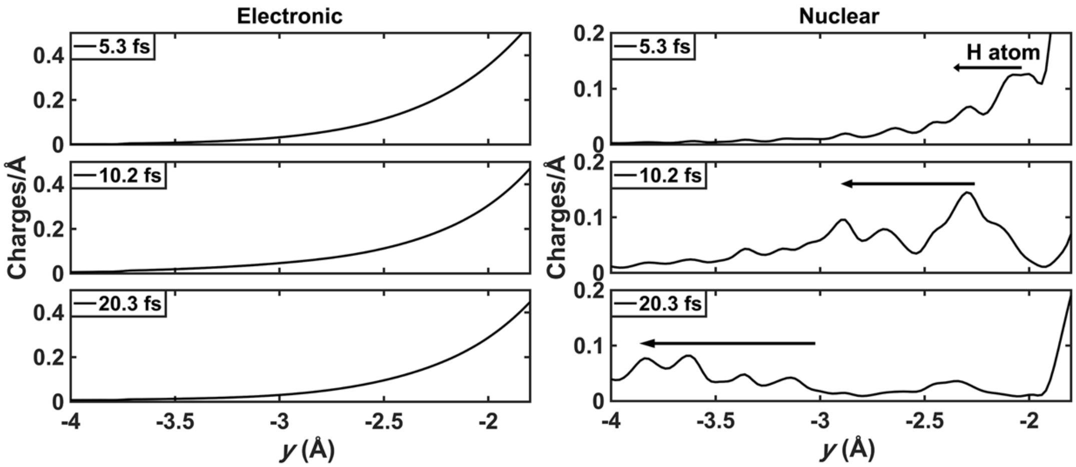

Figure S2. Real-space electronic (left) and nuclear (right) charge densities along the *y* axis at selected delay times. The charge densities are integrated over the *x* axis and the *z* axis for $z < -1$ Å.

Supplementary references

---

(1) Lim, I. S.; Lim, J. S.; Lee, Y. S.; Kim, S. K. Experimental and Theoretical Study of the Photodissociation Reaction of Thiophenol at 243 nm: Intramolecular Orbital Alignment of the Phenylthiyl Radical. *J. Chem. Phys.* **2007**, *126*, 034306.

(2) You, H. S.; Han, S.; Lim, J. S.; Kim, K. S. (ππ*/πσ*) Conical Intersection Seam Experimentally Observed in the S-D Bond Dissociation Reaction of Thiophenol-D_1, *J. Phys. Chem. Lett.* **2015**, *6*, 3202-3208.

(3) Werner, H.-J.; Knowles, P. J.; Manby, F. R.; Black, J. A.; Doll, K.; Heßelmann, A.; Kats, D.; Köhn, A.; Korona, T.; Kreplin, D. A.; et al. The Molpro Quantum Chemistry Package. *J. Chem. Phys.* **2020**, *152*, 144107.

(4) Werner, H. J.; Knowles, P. J.; Knizia, G.; Manby, F. R.; Schütz, M. Molpro: A General-Purpose Quantum Chemistry Program Package. *Wiley Interdiscip. Rev. Comput. Mol. Sci.* **2012**, *2*, 242-253.

(5) Sun, Q.; Berkelbach, T. C.; Blunt, N. S.; Booth, G. H.; Guo, S.; Li, Z.; Liu, J.; McClain, J.; Sharma, S.; Wouters, S.; et al. PySCF: the Python-Based Simulations of Chemistry Framework. *Wiley Interdiscip. Rev. Comput. Mol. Sci.* **2018**, *8*, e1340.

(6) Sun, Q.; Zhang, X.; Banerjee, S.; Bao, P.; Barbry, M.; Blunt, N. S.; Bogdanov, N. A.; Booth, G. H.; Chen, J.; Cui, Z.-H.; et al. Recent Developments in the PySCF Program Package. *J. Chem. Phys.* **2020**, *153*, 024109.

(7) Rouxel, J. R.; Kowalewski, M.; Bennett, K.; Mukamel, S. X-ray Sum Frequency Diffraction for Direct Imaging of Ultrafast Electron Dynamics. *Phys. Rev. Lett.* **2018**, *120*, 243902.

(8) Reiter, S.; Keefer, D.; de Vivie-Riedle, R. Exact Quantum Dynamics (Wave Packets) in Reduced Dimensionality. *Quantum Chemistry and Dynamics of Excited States*; Wiley, 2020; 355–381.

(9) Berens, P. H.; Wilson, K. R. Molecular Dynamics and Spectra. I. Diatomic Rotation and Vibration. *J. Chem. Phys.* **1981**, *74*, 4872–4882.

(10) Thallmair, S.; Roos, M. K.; de Vivie-Riedle, R. Design of Specially Adapted Reactive Coordinates to Economically Compute Potential and Kinetic Energy Operators Including Geometry Relaxation. *J. Chem. Phys.* **2016**, *144*, 234104.

(11) Tal-Ezer, H.; Kosloff, R. An Accurate and Efficient Scheme for Propagating the Time Dependent Schrödinger Equation. *J. Chem. Phys.* **1984**, *81*, 3967–3971.

(12) Butterworth, S. On the Theory of Filter Amplifiers. *Experimental Wireless and the Wireless Engineer* **1930**, *7*, 536–541.